Effect of Size and Structure on the Ground and Excited State Electronic Structure of TiO_2 Nanoparticles

Daeheum Cho,[a] Kyoung Chul Ko,[ab] Oriol Lamiel-García,[b] Stefan T. Bromley,[bc] Jin Yong Lee[a*] and Francesc Illas[b*]

[a)] *Department of Chemistry, Sungkyunkwan University, Suwon 16419, Korea*
[b)] *Departament de Ciència de Materials i Química Física & Institut de Química Teòrica i Computacional (IQTCUB), Universitat de Barcelona, c/ Martí i Franquès 1,08028 Barcelona, Spain*
[c)] *Institució Catalana de Recerca i Estudis Avançats (ICREA), 08010 Barcelona, Spain*

Abstract.

We investigated the influence of size and structure on the electronic structure of 0.5-3.2 nm diameter TiO_2 nanoparticles in both vacuum and water using density functional theory calculations. Specifically, we tracked the optical and electronic energy gap of a set of $(TiO_2)_n$ nanoparticles ranging from small non-bulk-like clusters with n =4, 8 and 16, to larger nanoparticles derived from the anatase bulk crystal with n = 35 and 84. As the difference between these two energy gaps (the exciton binding energy) becomes negligible in the bulk, this magnitude provides an indicator of the bulk-like character of the electronic structure of the nanoparticles under study. Extrapolating our results to larger sizes, we obtain a rough estimate of the nanoparticle size at which the electronic structure will begin to be effectively bulk-like. Our results generally confirmed that the electronic structure of nanoparticle ground state and excited state has a more pronounced structure dependency than size dependency within 0.5-1.5 nm size. We also showed that thermodynamic preference for the photocatalytic species is the first S_1 exciton. This S_1 exciton is stable in vacuum but may evolve to free charge carriers upon structural relaxation in an aqueous environment for 0.5-1.5 nm size particles studied in the present article. An analysis of ionization potentials and electron affinities relative to the standard reduction potential for the water splitting half-reactions revealed the importance of considering the structural relaxation in the excited states and the presence of water for assessing the thermodynamic conditions for photocatalytic water splitting.

* Corresponding authors: jinylee@skku.edu (J. Y. Lee). francesc.illas@ub.edu (F. Illas)

1. Introduction

Titanium dioxide (TiO_2), also referred to as titania, is widely studied by theory[1] and experiment[2,3] both with respect to its fundamental properties[2,3] and from a more applied perspective.[4] The latter interest in this material originates from the broad range of industrial applications ranging through solar cells,[5,6] environmental clean-up[7,8] and photocatalysis.[9-12] The applications of TiO_2 in photocatalysis constitute a particularly active field of research due to the possibility of generating H_2 from water splitting under light irradiation.[13,14] Because of the rather large band gap (> 3.0 eV)[15] of the most common polymorphs of titania (anatase and rutile), photocatalytic water splittictng using these materials requires ultraviolet (UV) radiation. This feature inhibits their practical use under sunlight as only ~10% of the sunlight incoming photons have enough energy to be absorbed and hence to participate in the photocatalytic process.

A number of different strategies have been used to modify the band gap of TiO_2 in order to increase its viable use with sunlight. Doping by different types of chemical elements, in particular with atomic nitrogen, has attracted much interest[16,17] However, some theoretical studies have shown that reducing the band gap to the visible range by introducing doping-induced defect states does not guarantee better catalytic performance.[18] For instance, heavily fluorine-doped anatase exhibits a clear blue color which electron paramagnetic resonance (EPR) measurements unambiguously attributes to Ti^{3+} centers.[19] However, in spite of these improved electronic properties, the photocatalytic activity of F-doped anatase in the visible remains quite modest. This example clearly highlights the difficulties encountered in the search for water splitting photocatalysts with sufficient activity in the visible.[19]

Nanostructuring has also been used to modify the photocatalytic activity of TiO_2. Of particular relevance to the present study, techniques have been developed for a control of the shape and size of titania nanoparticles in order to optimize them for

photoactivity.[20] However, in such experiments, it is difficult to discern between the different effects of size and shape and those introduced by the synthetic conditions. Lu et al.[21] have shown, for example, that F-doping largely stabilizes the (001) reactive facets of anatase, a feature that has been explained by *ab initio* thermodynamic arguments based on density functional theory (DFT) calculations.[22] However, as mentioned above,[19] F-doping also introduces Ti^{3+} centers. The intertwined influences of F-doping thus make it difficult to assign any resulting change in reactivity to either the presence of the particular enhanced structural feature or the new chemistry of the resulting nanomaterial.

The difficulties encountered by experiments to separate complex factors are not present when employing theoretical models in which one can represent different morphologies for a given composition or vary the composition for a given morphology. However, modeling the structure of TiO_2 nanoparticles of an experimentally relevant size using first-principles electronic structure methods is still a huge challenge, and even more so if the goal is to determine excited states and their properties. To overcome this difficulty a large amount of work has used extended models for TiO_2 bulk polymorphs[18, 23 - 30] and several surfaces[31 - 33], where the computational cost is significantly reduced by imposing periodic boundary conditions. The use of these models has provided a large amount of useful information but effects arising from the finite size and shape of the TiO_2 nanoparticles are largely missing. To help close the gap between such periodic models and small nanocluster models, Barnard et al.[34] developed a self-consistent tight-binding (SCTB) model that was found to be able to mimic the results obtained from DFT calculations of a moderately sized $(TiO_2)_{35}$ nanoparticle. This approach was then subsequently employed to investigate the stability and atomic structure of $(TiO_2)_n$ particles with *n* up to 455 (i.e. 1365 atoms) having different realistic bulk-cut morphologies. Nevertheless, a more accurate description of the electronic

structure properties of these large nanoparticles has yet to be attempted. Auvinen et al.[35] carried out DFT and time-dependent DFT (TD-DFT) calculations for $(TiO_2)_n$ particles with selected sizes in the range n = 8-38. They showed that the electronic structure of the studied TiO_2 nanoparticles strongly depends on the atomic structure and also that constraining small nanoparticles to possess a bulk-like atomic structure is very likely to yield metastable structures with respect to the most stable structural ground states, which are typically non-bulk-like. In other reported studies specifically searching for low energy $(TiO_2)_n$ clusters, those with sizes up to n = 16 are indeed found to not display the anatase crystal structure.[36,37,38,39] Rather, small to moderately large $(TiO_2)_n$ nanoclusters typically exhibit a significant number of non-bulk-like energetically low lying isomers. Since this implies that experimental measurements may provide information over an ensemble of particles rather than on the most stable structural ground state, it is necessary to investigate the properties of different isomers of TiO_2 nanoparticles. This is analogous to the bulk case of TiO_2 polymorph engineering, where similarly energetically stable yet distinct crystal structures lead to different modifications of band edges and the hence band gaps due to varying local coordination.[40] The ground state and excited electronic structure of specific low energy $(TiO_2)_n$ non-bulk-like clusters in the size range n =1-15 have been studied in detail,[41,42] but information regarding larger particles is almost inexistent. Therefore, the aim of the present work is to provide a bridge between these two ranges through a unified consistent theoretical examination of how the ground state and excited electronic structure evolves from non-bulk-like clusters to bulk-structured nanoparticles considering several different isomers of the smaller clusters.

Using DFT and TD-DFT methods we have explored the electronic structure properties of the ground and excited states of $(TiO_2)_n$ with n = 4, 8, 16, 35 and 84 resulting in nanoparticles containing up to 252 atoms and reaching ~3 nm in diameter.

We show that while energetic stability tends to monotonically increases with size, the corresponding electronic structure can vary significantly depending on the structure and shape of nanoparticle. To investigate the size-dependent change in electronic structure we focus on the optical and electronic energy gaps. In particular, we use the difference between these two energy gaps (i.e. the exciton binding energy) as a measure of how bulk-like a cluster of a certain size is with respect to its electronic structure. For the range of nanoparticles studied, we will also show that, in vacuum, the exciton state is always more stable than free charge carriers and that this hold for both vertical and adiabatic time scales, whereas solvation may reverse this order. Finally, we present a thermodynamic analysis with respect to the necessary, but not sufficient, conditions for spontaneous water splitting triggered by photoexcited TiO_2 nanoparticles in vacuum and in water.

2. Electronic structure properties

The band gap of TiO_2 materials is one of the key properties enabling their technological applications either in photocatalysis or in solar cells. Hence, it is important to recall that there are two well-defined ways to determine the band gap of a material; often referred to as the electronic or fundamental gap and the optical band gap, respectively.[43] The electronic (or fundamental) band gap is measured by (direct and inverse) photoemission experiments and thus involves charged states either of cationic (free extra hole, h^+) or anionic (free extra electron, e^-) character. On the other hand, the optical band gap is obtained by photoexcitation process that generates an excited electron-hole (e^--h^+) pair, so called exciton pair. In the case of relatively small finite systems, the optical band gap is lower than the electronic band gap due to the electrostatic stabilization of the electron-hole pair interaction in the exciton state. However, for large systems including bulk or extended surfaces, the difference between

electronic and optical gaps typically becomes negligible since the addition/removal of one electron to/from fully delocalized states in the infinite solid will not significantly affect its electronic structure. A difference can be found when, due to the specific electronic structure features, the excess electron and/or hole involve localized states forming a well-defined exciton. In fact, small exciton-like excitations have been found in rutile and anatase but the corresponding excitation energies are of the order of a few meV.[44-46]

As the concept of a band for a finite system is ill defined, we will hereafter use the term "energy gap" for TiO_2 nanoparticles, which corresponds to "band gap" for surface or bulk. We denote the electronic energy gap as "E_{gap}" and the optical energy gap as "O_{gap}" in order to distinguish the two different kinds of energy gap. A rough estimate of the E_{gap} can often be obtained from the difference between the orbital (Hartree-Fock or Kohn-Sham) energy of the highest occupied molecular orbital (HOMO) and that of the lowest unoccupied molecular orbital (LUMO); hereafter this quantity will be denoted as $\Delta E_{H\text{-}L}$ = E(LUMO) – E(HOMO). These values show a strong dependence on the choice of the exchange-correlation functional, because they depend solely on the ground state one-electron Kohn-Sham eigenvalues. A more reliable method to estimate E_{gap} consists in taking the energy difference between the vertical ionization potential (IP_v) and electron affinity (EA_v) (See equations 2, 4, and 5).

The O_{gap} is obtained from the S_0 ground to S_1 excited state $(S_0 \rightarrow S_1)_v$ vertical excitation which involves the creation of an exciton in the S_1 state (See equation 3). We note that in some cases the lowest triplet T_1 state is used instead of S_1 to define the optical gap. In the present work we will focus mainly in the $(S_0 \rightarrow S_1)_v$ electronic transition (similar results are found for the $(S_0 \rightarrow T_1)_v$ excitation, as shown in the Supporting Information Tables S1 and S2).

Another important quantity is the so-called exciton binding energy (ΔE_{ex}) defined as

$$\Delta E_{ex} = E_{gap} - O_{gap} \quad (1),$$

which provides an estimate of e^--h^+ pair interaction energy in the S_1 exciton state compared to free charged particles. In the following, we will use the notation introduced earlier by Guiglion et al.,[47] also employed in subsequent works by some of these authors.[48,49] Thus, for a particle P we will use E(P) to denote the energy of the ground state S_0 at the optimized geometry and $E(P^*)$, $E(P^+)$, $E(P^-)$ to denote the energies of S_1, cationic and anionic states at the S_0 optimized geometry, respectively. One then has,

$$E_{gap} = IP_v - EA_v \quad (2)$$

$$O_{gap} = (S_0 \rightarrow S_1)_v = E(P^*)_v - E(P) \quad (3)$$

$$IP_v = E(P^+)_v - E(P) \quad , \quad IP_{ad} = E(P^+)_{ad} - E(P) \quad (4),$$

$$EA_v = E(P) - E(P^-)_v \quad , \quad EA_{ad} = E(P) - E(P^-)_{ad} \quad (5),$$

where "v" and "ad" subscripts hereafter, denote vertical (using S_0 geometry only) and adiabatic (using the relaxed geometry of each species at each electronic state) quantities, respectively. Accordingly, one can define vertical and adiabatic exciton binding energy values which takes the form

$$\Delta E_{ex,v} = [E(P^+)_v + E(P^-)_v] - [E(P^*)_v + E(P)] \quad , \quad (6)$$

$$\Delta E_{ex,ad} = [E(P^+)_{ad} + E(P^-)_{ad}] - [E(P^*)_{ad} + E(P)] \quad (6')$$

which formally corresponds to the energy change associated to the hypothetical process:

$$P + P^* \rightarrow P^- + P^+ \quad (7)$$

therefore, $\Delta E_{ex,v}$ and $\Delta E_{ex,ad}$ provide a measure of the stability of the exciton relative to free charge carriers in vertical and adiabatic time scales, respectively. With the definitions in (6) and (6'), a positive value of ΔE_{ex} indicates that the exciton is more stable than free charge carriers.

3. Selected TiO_2 nanoparticles and computational details

The primary goal of the present manuscript is to reveal how the ground and excited state electronic structure and derived properties vary with the size and the shape of TiO_2 nanoparticles. We also studied photocatalytic requirements in a thermodynamic sense, and estimation of excited state lifetimes of these nanoparticles. A set of $(TiO_2)_n$ nanoparticles with *n* = 4, 8, 16, 35 and 84 was selected encompassing systems containing up to 252 atoms (~ 3 nm in diameter). For the selection of the smaller particles we have been inspired in the recent works of Zwijnenburg and coworkers,[42,47,48] whereas for the larger TiO_2 nanoparticles we rely on the previous work of Barnard et al.[34]

Regarding the selection of the small nanoparticles, we know from previous work that excitation (or photoemission) energy of $(TiO_2)_n$ with n = 2, 5, 10 calculated by B3LYP functional show serious deviation from values obtained with the CAM-B3LYP functional.[38,42,48] Hence, we selected non-bulk-like $(TiO_2)_n$ clusters with n=4,8,16, where CAM-B3LYP and B3LYP yielded qualitatively similar results; we also added structures of several lowest isomers which are well studied. The particles with *n* = 4, 8 and 16 thus chosen have structures with little resemblance to bulk anatase and thus correspond to the so-called non-scalable (i.e. not having properties that can be simply scaled from bulk values) regime (see Figure 1, left). On the contrary, the larger particles with *n* = 35 and 84 exhibit clear bulk-like structure and can be taken as representative examples of particles in the scalable regime (see Figure 1, right). For the particles with *n* = 4-16, the structural effect of these nanoparticles on the electronic structure was also investigated by choosing four different isomers (a-d) for each selected *n* values, since exploring all stable isomers for relatively large TiO_2 nanoparticles is effectively intractable. Electronic structures of ground and excited states in the $(TiO_2)_4$ and $(TiO_2)_8$ were studied by many authors and it is known that, for

these nanoparticles, DFT and TD-DFT approaches with hybrid functionals work well. On the other hand, it is known that theoretical calculations employing the pure Generalized Gradient Approximation (GGA) to the exchange-correlation potential have difficulties in describing the electronic structure of oxides and other strongly correlated materials[1,18]. Thus, we employed B3LYP[50] and CAM-B3LYP[51] hybrid functionals, which incorporate a certain fraction of Hartree-Fock exchange. The corresponding calculations for ground and excited state electronic structure properties have been carried out using a 6-31G(d) basis sets and the Gaussian09[52] suite of programs.

The initial geometry of the structural ground state (a) and of the three higher energy isomers (b to d) of the $(TiO_2)_4$ and $(TiO_2)_8$ particles were taken from Marom et al.[38] For the $(TiO_2)_{16}$ particle, the candidate ground state and the rest of isomers were generated using Monte Carlo basin hopping[53] global optimization using a mixed interatomic potential based strategy employed in previous work.[37] In order to minimize the variance in energetic stability our isomers for each size *n* we chose low energy isomers that were within 0.16 eV total energy per unit of the lowest energy isomer found, calculated at a B3LYP/6-31G(d) level in vacuum. Specifically, isomers were taken within the energy ranges +0.143, +0.130, +0.156 eV per TiO_2 unit for sizes $n = 4$, 8 and 16, respectively.

The structures of bulk-like particles $(TiO_2)_{35}$ and $(TiO_2)_{84}$ were selected based on bi-pyramidal Wulff cuts[54] from the anatase bulk crystal. We found $(TiO_2)_{35}$ is the smallest Wulff cut nanoparticle that preserves anatase (101) facets after geometrical relaxation. For the $(TiO_2)_{35}$, two slightly different geometries were used: (i) a B3LYP/6-31G(d)/Gaussian09 optimized structure starting from the anatase bulk cut structure optimized using SCTB as reported by Barnard et al.[34] ($(TiO_2)_{35a}$), and (ii) a PBE/tier-1/FHI-aims [55] optimized structure starting from the Wulff cut from experimental anatase bulk exhibiting (101) facets ($(TiO_2)_{35b}$). We note that, apart from

the tilting of the apical O atoms, the two $(TiO_2)_{35}$ structures obtained from the (i) and (ii) are quite similar with the difference in total energy calculated at the B3LYP/6-31G(d) in vacuum being of 1.609 eV (0.046 eV per TiO_2 unit). Finally, for the largest $(TiO_2)_{84}$ nanoparticle reaching 3 nm in size, the structure was optimized also using the FHI-aims code at the PBE/tier-1 level from an anatase bulk cut exhibiting (101) facets ($(TiO_2)_{84a}$). In the forthcoming discussion we will refer to results for the two types of structures following the standard method//structure notation. Consequently, B3LYP/6-31G(d)//B3LYP/6-31G(d) denotes calculations at the B3LYP/6-31G(d) level of theory at the structure optimized with the same method, and B3LYP/6-31G(d)//PBE-tier1 refers to calculations at the B3LYP/6-31G(d) level of theory but using the structures obtained from geometry optimization using PBE/tier-1 basis set.

For each of the structures, the IP, EA, E_{gap}, O_{gap} and ΔE_{ex} values were obtained at two different level of theories B3LYP/6-31G(d) and CAM-B3LYP/6-31G(d) using the Gaussian09 code for comparison. The CAM-B3LYP functional was chosen as it was designed to provide relatively improved results for excitations regarding charge-transfer character.[51] For the B3LYP, the Tamm-Dancoff approximation (TDA)[56] was used to reduce the instability of excited states in the calculations involving the larger clusters. Nevertheless, test calculations for the small $(TiO_2)_n$ particles (n = 4, 8, 16) indicate that the O_{gap} values obtained at TDA-B3LYP and TD-B3LYP levels differ by less than 0.005 eV. For the CAM-B3LYP calculations, TDA was not found to be necessary.

In addition, we considered solvation effect of TiO_2 nanoparticles by water (dielectric constant ε = 78.3553) by using the implicit conductor-like polarizable continuum model (CPCM)[57] to estimate the thermodynamic driving force to facilitate water splitting half-reactions, i.e., hydrogen (HER) and oxygen evolution (OER) at pH = 7. Several reports in the literature explicitly consider water solvent molecules and

hydration/hydroxylation of TiO_2 surfaces.[42,58,59,60,64] This is because the defect sites of TiO_2 surfaces, such as mono-coordinated oxygen and three-coordinated titanium atoms, are highly prone to be protonated/hydrated to stabilize the system (exothermic process) when immersed in water. It is clear that the approximate nature of the CPCM method cannot account for local (and explicit) water solvation effects and hydration of the possible defect sites, which may be especially important for the small nanoparticles studied in the present work. Nevertheless, we argue that CPCM may qualitatively capture some of the most important features of water solvation such as dielectric screening of electrostatic interaction, which is critical to describe e^-–h^+ interaction energy in the exciton state and spatial distributions of molecular orbitals. Indeed, significant and sensible changes in half-reaction potentials of the TiO_2 nanoparticles upon water solvation were found in the present study, which are useful to understand the effect of the solvation, at least in a qualitative way. It is also interesting to note that the ranges of the half-reaction potentials in CPCM water model in the present study do well correspond to those of rutile nanocrystals immersed in explicit water environment with hydrated surfaces.[42] However, we also note that the results obtained by CPCM model artificially affect some properties such as localization of free electron/hole in the (unhydrated) structural defects such as under-coordinated titanium/oxygen as shown in Figures S8-11. This caveat applies to all the CPCM related results and discussions presented throughout the paper.

4. Results and discussion

4.1 TiO_2 nanoparticle structure

From Figure 1 it is quite clear that the structure of small nanoparticles containing 4-16 TiO_2 units have many under-coordinated Ti and O atoms and little resemblance to the bulk structure, a feature that is well-known for small clusters of metal oxides.[61] In these

cases, the size of the particle is not large enough to build a Madelung field, which is an important component defining the stability of the structure of bulk polymorphs. Small $(TiO_2)_n$ (i.e. for n =4, 8 and 16 in our study) nanoparticles made from symmetric cuts from the bulk anatase polymorphs are expected to be highly metastable with respect to our correspondingly sized lowest energy clusters. Taking as an example, the $(TiO_2)_{16}$ nanoparticle derived from the anatase bulk by Persson et al.[62], the optimized structure maintains a distorted anatase structure but at this size it cannot display well-defined low index surfaces. The total energy difference between our candidate ground state and this structural isomer is also found to be quite large (4.867 eV or 0.304 eV per TiO_2 unit) at a B3LYP/6-31G(d) level in vacuum, and clearly outside of our considered stability range. A different situation is encountered for our larger $(TiO_2)_{35}$ nanoparticle which displays a relatively unperturbed anatase structure, and exhibits clear (101) facets.[34] Clearly, this nanoparticle can be regarded as a true anatase nanocrystal, although at present we do not have good knowledge of other possible energetically competing isomers in this size range to assess its corresponding energetic stability.

Figure 2 reports the trend in stability for the different particles taking into account size, shape and structure as obtained from B3LYP/6-31G(d) calculations in vacuum. We note that similar trends are found for the results in water and for those obtained at the B3LYP/6-31G(d) level either in vacuum or water as we report in the Supporting Information (Table S3). The plot in figure 2 shows the expected monotonic decrease of the total energy per unit for the our lowest energy $(TiO_2)_n$ nanoparticles for n =4, 8 and 16 units, and for the optimized bulk cuts with 35 and 84 units. Ideally, one would need to use the bulk value obtained with the same methods and basis set as a reference. However, as we performed our calculations with a local basis set using a DFT code developed for non-periodic calculations, this implies several technical problems and we found it convenient to use the value for the largest particle as the reference.

Figure 2 shows the steep descent in energetic stability for the smaller particles and the smoother leveling off in stability for the largest ones. The range of energy per TiO_2 unit spanned for the different isomers is indicated by a vertical shaded bar.

4.2 Electronic structure of TiO_2 nanoparticles in vacuum

We first analyze the electronic structure of the small $(TiO_2)_n$ nanoparticles for n = 4, 8 and 16 as a function of shape and size in vacuum and as predicted by the B3LYP/6-31G(d)//B3LYP/6-31G(d) calculations. Qualitatively, both O_{gap} and ΔE_{H-L} follow similar trends (See Supporting Information Table S4 for ΔE_{H-L}) with respect to their dependency on structure for each size and changes in size. Moreover, for the lowest energy structures of the $(TiO_2)_4$ and $(TiO_2)_8$ nanoparticles, the present values for O_g are similar to those reported by Berardo et al.[42] using also the B3LYP functional. For the $(TiO_2)_{35}$ bulk-cut nanoparticle the O_{gap} calculated using B3LYP/6-31G(d) depends somewhat on the chosen structure; 3.67 eV for the B3LYP/6-31G(d) optimized structure and 3.36 eV for the PBE/tier-1 optimized structure. Hence, the effect of the DFT method used to optimize the structure on the calculated O_{gap} is 0.31 eV or ~10%. For the largest $(TiO_2)_{84}$ particles, the B3LYP/6-31G(d) value of O_{gap} employing the PBE/tier-1 optimized structure is 3.40 eV.

We note that the O_{gap} values are 0.38 – 1.16 eV lower than the corresponding ΔE_{H-L} ones, this is simply a result of having the LUMO singly occupied in the S_1 excited state and of the concomitant stabilization through the electron-hole pair interaction. Interestingly, the ΔE_{H-L} value for $(TiO_2)_{84}$ is 4.02 eV, which is close to the band gap of 3.92 eV computed for bulk anatase by Finazzi et al.[27] using the B3LYP functional and a periodic model. Nevertheless, this comparison has to be taken with caution since, as shown below, convergence to bulk electronic properties involves rather larger nanoparticle sizes. Figure 3 also reveals that the O_{gap} of the investigated TiO_2

nanoparticles exhibit a large dependence on the nanoparticle structure and a smaller one on the size. On the other hand, the E_{gap} values decrease significantly with the particle size. This is likely due to the free charge carriers (cationic and anionic nanoparticles) being relatively more stabilized through spatial delocalization of the electron (e^-) or hole (h^+) in the larger nanoparticles. Nevertheless, the dependence of E_{gap} on nanoparticle structure can be significant for the smaller cluster and is found to vary by up to 2.3 eV for both $(TiO_2)_4$ and $(TiO_2)_{16}$. In the case of $(TiO_2)_8$, however, the range of E_{gap} values spanned by the different isomers is much narrower.

At the CAM-B3LYP/6-31G(d) level of theory, the size and structure dependency of O_{gap} and E_{gap} are almost quantitatively identical to that for B3LYP/6-31G(d) discussed above indicating that these trends are, to some extent, independent of the hybrid DFT method employed. Although the CAM-B3LYP functional only yields slightly larger values of both O_{gap} and E_{gap} values compared to B3LYP, it provides ΔE_{H-L} values that are about 3 eV higher than those from B3LYP; a drawback of CAM-B3LYP previously reported by several authors.[63] This difference in the ΔE_{H-L} values does not seem to represent a problem since the physically meaningful O_{gap} values predicted by B3LYP and CAM-B3LYP in vacuum are quite similar. Note also that reported CAM-B3LYP calculated values for photoluminesence of TiO_2 nanoparticles correspond well to experimental data.[48,64]

4.3 Electronic structure of TiO_2 nanoparticles in water

The effect of water as a solvent, as included using the CPCM method, leads to a dramatic change in the calculated O_{gap} values (see Figure 4). Notably, a rather large reduction of the O_{gap} dependence on cluster isomer structure with respect to the non-solvated calculations (see Figure 3 for comparison) is predicted from the TD-DFT calculations using both B3LYP/6-31G(d) and CAM-B3LYP/6-31G(d) methods. This

phenomenon is probably due to the dielectric screening of specific charge localization patterns of extra electron and hole species on each isomer (see Supporting Information Figure S1). In this context, significant lowering of E_{gap} can also be expected and understood. Overall, the O_{gap} and E_{gap} values in water slightly decrease as the size of the TiO_2 nanoparticle increases.

4.4 Dependence of the exciton binding energy on nanoparticle size and shape

In Section 2, we argued that the exciton binding energy (ΔE_{ex}) can be taken as a measure of electron-hole pair interaction in the excited state and of the stability of excitons relative to free charge carriers. Figure 5a shows vertical exciton binding energies $\Delta E_{ex,v}$ for all TiO_2 nanoparticles in vacuum and in water as predicted from DFT and TD-DFT calculations using the B3LYP and CAM-B3LYP functionals whereas Figure 5b reports the CAM-B3LYP results for the adiabatic ΔE_{ex} values for the particles containing up to 16 units. For the vertical ΔE_{ex} values, both B3LYP and CAM-B3LYP functionals provide qualitatively and quantitatively similar results except for slight deviation in small nanoparticles in vacuum. The adiabatic ΔE_{ex} values in Figure 5b correspond to results obtained with the CAM-B3LYP method since the B3LYP calculations exhibited a computational instability for geometry relaxation in excited state with charge transfer character.[42]

4.5 Relative stability of S_1 excitons and free charge carriers.

A very important feature in Figure 5b is that exciton binding energy of the TiO_2 nanoparticles in water becomes negative after geometry relaxation. Hence, at the CAM-B3LYP level, one gets vertical ΔE_{ex}(water) > 0 eV and adiabatic ΔE_{ex}(water) < 0 eV. In other words, the stabilization through structural relaxation in the free charge carrier state is larger than that in the S_1 exciton state. This indicates that under irradiation, photocatalytic species initially stable as an S_1 exciton pair may evolve to

free charge carriers upon structural relaxation in water environment. Considering that the excited state lifetime for bulk anatase) is ~10 ns[65,66,67] one can safely argue that a similar time scale will apply for TiO_2 nanoparticles. This seems to be sufficient to allow for structural relaxation in the excited state which has important consequences. In fact, it would be especially meaningful that free charge carriers may become abundant and do play an important role during the photocatalytic reaction in water; a picture that contrasts with the purely thermodynamic point of view favoring the S_1 exciton species.

To further verify that lifetime of excited states in TiO_2 nanoparticles is large enough so as to allow for structural relaxation, calculated excited state lifetime (τ) have been calculated. This span a rather wide range (0.05 – 50 μs) of time scales depending on the sizes and structures of the TiO_2 nanoparticles studied; details regarding the calculation of lifetimes and the corresponding values are reported in Figures S6, S7 and Tables S12 to S17 of the Supporting information. Hence, structural relaxation in the S_1 exciton state may occur before electronic decay. It is also worth to note that the S_1 lifetime in water is significantly smaller than in vacuum due to the dielectric screening of the electron-hole interaction and transition dipole moment from S_0 to S_1. Considering that the calculated lifetime values in the present work are significantly longer than experimental reports for bulk and surface,[65-67] non-radiative decay would be a much faster process than radiative decay, which is consistent with report by Zwijnenburg for hydrated rutile nanocluster in water[64]. Yet, the calculated lifetime in the present work is much shorter than the prediction for the hydrated nanocluster (0.2 - 3 ms)[64] indicating that non-radiative decay would become dominant for these systems.

In contrast, in vacuum, the S_1 exciton state is more stable than the free charge carriers state regardless of the structural relaxation, both vertical ΔE_{ex}(vacuum) > 0 (for up to $(TiO_2)_{84}$) and adiabatic ΔE_{ex}(vacuum) > 0 eV (for up to $(TiO_2)_{16}$) (Figures 5a and 5b). These different thermodynamic preferences among free charge carrier and S_1

exciton states upon structural relaxation— $S_1 \rightarrow S_1$ in vacuum but $S_1 \rightarrow$ free charge carriers in water— in conjunction with their redox potentials relative to water splitting half-reactions has important implications on the determination of the photocatalytic ability of TiO_2 nanoparticles (See Section 4.5.).

4.6 Size and shape dependence of exciton binding energy.

Figure 5a, shows that vertical ΔE_{ex} sharply decreases as the number of TiO_2 units increases, which is primarily due to the behavior of E_{gap} (vacuum) as shown in Figure 3. This indicates that the electrostatic electron-hole pair interaction energy in a large $(TiO_2)_{84}$ nanoparticle is small which is probably due to the large electron-hole distance and/or to the delocalized character of both electron and hole. The latter effect is evidenced by weak electron-hole densities for larger nanoparticles as shown in Supporting Information (Figures S8-11). The plot of $\Delta E_{ex,v}$(vacuum) as a function of the number of TiO_2 units in Figure 6a is found to be well fitted by an inverse power law of the form:

$$\Delta E_{ex,v}(\text{vacuum}) = 7.16n^{-0.3} \qquad (R^2 = 0.99) \qquad (7)$$

revealing that the initial rapid decline of ΔE_{ex} with the nanoparticles size becomes more gradual for larger nanoparticles. For example, the difference in ΔE_{ex}(vacuum) going from $(TiO_2)_4$ to $(TiO_2)_{84}$ (2.87 eV) is much larger than that between $(TiO_2)_{84}$ and $(TiO_2)_{500}$ (estimated as 0.80 eV), indicating a significant quantum confinement effect for particles with sizes below ~100 units (ca. ~ 3 nm size). This is likely to result from a relatively strong electrostatic electron-hole pair interaction in small nanoparticles. Assuming that the extrapolation of ΔE_{ex}(vacuum) holds for larger particles, one can estimate the point at which the electrostatic electron-hole pair interaction in an S_1 exciton becomes similar to that of free charge carriers. At this point $\Delta E_{ex}(\text{vacuum}) \approx 0$ and one can safely argue that the electronic structure of the nanoparticle becomes

practically bulk-like. Taking a typical experimental error to be approximately 0.1 eV, when the difference in measured energy gaps is ≤ 0.2 eV the optical and fundamental gaps are assumed to be effectively indistinguishable in magnitude and both bulk like. We thus take the size at which the exciton binding energy is 0.2 eV to be indicative of the smallest size at which a TiO_2 nanoparticle exhibits a bulk-like electronic structure. Using equation 7 and plotting the exciton binding energy against $n^{-0.3}$ we can extrapolate from our data to give an estimate of this bulk onset size to be ~15000 units (~20 nm apical diameter in an anatase bipyramidal nanoparticle), see Fig. 6b. This is rather large and is actually at a size when anatase nanoparticles are predicted to become metastable to rutile nanoparticles, implying that only relatively large metastable anatase nanoparticles would display a saturated bulk-like electronic structure.[68] We note, however, that this estimate is dependent on the functional employed. This is especially so with respect to the optical gap magnitude, which is particularly sensitive to the degree of non local Fock exchange introduced in the functional.[69] In our case the B3LYP functional is known to overestimate the band gap of bulk anatase by 23%.[27] Assuming a similar overestimate of the optical gap in our TD-DFT B3LYP calculations for our large bulk like nanoparticles we can make an approximate correction to the extrapolated nanoparticle size at which the electronic structure becomes bulk-like. In Fig 6b we show that the corrected extrapolated size becomes $(TiO_2)_{930}$ (~6.5 nm apical diameter in an anatase bipyramidal nanoparticle). Although, this value clearly rests upon some assumptions we present it at reasonable estimate of the lower size limit at which anatase nanoparticles start to become bulk-like with respect to their electronic structure.

4.7 Relevance to Photocatalytic Water Splitting.

It is interesting to relate the presence of free charge carriers and S_1 exciton

states as possible driving forces for the photocatalytic water splitting reaction, at least from a thermodynamic point of view. Recently, many theoretical attempts have been made to evaluate the photocatalytic capability of semiconducting materials. Such calculations have focussed on properties such as the band edge (valence band maximum and conduction band minimum) for bulk and surfaces,[40,75,76] or the IP and EA of nanoparticles and clusters.[70,71] Comparing these quantities with standard reduction potentials of water splitting half-reactions, one can obtain a rough estimate of the necessary thermodynamic conditions for the photocatalytic capability of an anatase catalyst.

The water splitting reaction driven by photo-excited TiO_2 nanoparticles involves the hydrogen evolution reaction (HER) and the oxygen evolution reaction (OER) redox processes; where TiO_2 nanoparticles in free charge carrier and/or S_1 exciton states are the source for electrons and holes, respectively. The corresponding redox reactions for hole/electron generation in TiO_2 nanoparticles from free charge carriers are defined in equations 4 and 5. Here we note that IP/EA of anionic/cationic TiO_2 particle were employed to simulate the redox behaviors of free electron/hole in free charge carriers by assuming negligible electron-hole interactions. Here we define similar quantities for the S_1 exciton.

$$IP_v^* = E(P^+)_v - E(P^*)_v \quad , \quad IP_{ad}^* = E(P^+)_{ad} - E(P^*)_{ad} \qquad (8)$$

$$EA_v^* = E(P^*)_v - E(P^-)_v \quad , \quad EA_{ad}^* = E(P^*)_{ad} - E(P^-)_{ad} \qquad (9)$$

which correspond to the dissociation of bound electron through the electron transfer processes involving the S_1 (P^*) exciton state

$$P^* \rightarrow P^+ + e^- \qquad (10)$$

$$P^* + e^- \rightarrow P^- \quad (11)$$

We also note that IP* = IP – ($S_0 \rightarrow S_1$) and EA* = EA + ($S_0 \rightarrow S_1$).

Following previous work,[64,72] it is possible to relate the $IP^{(*)}/EA^{(*)}$ values to the experimental value for the potential of the standard hydrogen electrode (SHE) potential (4.44 eV)[73,74], by subtracting 4.44 eV from the calculated $IP^{(*)}/EA^{(*)}$ values for the free carrier and exciton states, respectively. In fact, for the photocatalytic HER and OER to take place, redox potentials of each half-reaction and photocatalytic TiO_2 reduction and oxidation should be in a suitable order. Hence, each pair of IP/EA and (or) IP*/EA* values should be well separated from the potentials of the half-reactions, one above (i.e. more negative than) the HER and the other below (i.e. more positive than) OER standard reduction potential so that HER and OER half-reactions spontaneously receive e^- and h^+ via redox pair reactions, respectively (See Figure 7). From this comparison it is then possible to obtain the trends for the photocatalytic capability of free charge carrier and S_1 exciton species towards HER and OER half-reactions at pH = 0 and 7 (See also Ref 70 and 71 for further details on these concepts). It would be also interesting to investigate the dynamical behaviors of the photocatalytic capabilities of TiO_2 nanoparticles by comparing the standard redox potentials in the vertical and adiabatic time scales, i.e., $IP_v^{(*)}/EA_v^{(*)}$ and $IP_{ad}^{(*)}/EA_{ad}^{(*)}$, respectively. Indeed, dynamical aspects of photoexcited TiO_2 nanoparticles are of great importance because the excited state lifetime of TiO_2 nanoparticles and standard chemical reactions are long enough to allow the carrier relaxation in the excited state. The vertical and adiabatic $IP^{(*)}/EA^{(*)}$ potentials of the nanoparticles in water calculated by CAM-B3LYP/6-31G(d) are reported in Figure 8 (a similar trend is predicted when employing B3LYP, see Supporting Information Figures S2 to S4 and for full results for the standard reduction potentials calculated by CAM-B3LYP in vacuum and water see Tables S8 to S11). The

absolute values (not relative to SHE potential) of IP_v (9.2 – 11.0 eV) and EA_v (1.5 – 3.3 eV) potentials in the TiO_2 nanoparticles in vacuum calculated by CAM-B3LYP/6-31G(d) level are much higher and lower than the corresponding IP_v (7.82 – 8.30 eV) and EA_v (4.67 – 5.10 eV) potentials for periodic TiO_2 anatase,[40,75,76] probably due to the quantum confinement effect in the TiO_2 nanoparticles. Furthermore, direct comparison of the vertical and adiabatic $IP^{(*)}/EA^{(*)}$ potentials of our nanoparticles in water calculated by CAM-B3LYP/6-31G(d) level with those of hydrated rutile nanocrystal immersed in explicit water molecules in Ref 64 confirm the validity of the present results (see Supporting Information Table S9).

To facilitate the discussion, we will first consider the properties of the particles in vacuum. This is just for completeness and for comparison purposes since water splitting in vacuum is physically meaningless. In short, only free charge carriers, which is metastable species in vacuum (Figure 5a and 5b, left panels), have photocatalytic capabilities, whereas S_1 exciton has no driving force for HER due to the too high EA*, i.e., low LUMO energy (see Supporting Information Figure S2). Hence, TiO_2 nanoparticles studied are incapable of photocatalytic water splitting in vacuum. Regarding the effect of the size and shape of the nanoparticles, one can barely see a significant trend in the potentials; excepting slight upwards/downwards trend of IP_v/EA_v as a function of the size (Figure S2a top).

The presence of water, taken into account in the CPCM solvent model, significantly changes the trend noted above. Result in Figure 8a show that a water solvent leads to lowering/lifting of IP/EA potentials of free charge carriers due to electrostatic stabilization of positive holes/negative electrons, respectively. Since IP values are found to be more affected than EA values, photocatalytic OER driven by free charge carrier becomes less exothermic. On the contrary, a water solvent leads to lifting/lowering of IP*/EA*, because the energy stabilization in the S_1 exciton is smaller

than that of free charge carriers (Figure 8b). Hence, the presence of water shifts the IP*/EA* potentials to the point of enabling photocatalytic water splitting driven by the S_1 exciton. Therefore, most of the small TiO_2 nanoparticles in both free charge carrier and S_1 exciton states are expected to have photocatalytic capability for water splitting even though some of them are incapable of the HER. Regarding the effect of the size and shape of the nanoparticles, one can only see a slight downward trend of EA_v potentials as a function of the particle size.

According to the thermodynamic analysis of $IP^{(*)}/EA^{(*)}$ potentials and to the energetic stability between free charge carriers and the S_1 exciton, one may argue that vertically generated S_1 exciton first facilitates the photocatalytic reaction and then free charge carriers become main contributor to the reaction. It is, however, very difficult to determine the major contributor throughout the whole reaction, because to track time-resolved dynamics of excited state relaxation when free charge carriers become more abundant than S_1 excitons is not at all trivial within the standard TD-DFT framework. Therefore, the dynamics regarding the excited state decay and the electron transfer processes in the course of photocatalytic water splitting of TiO_2 nanoparticles remain as key issues to be solved. Another challenge is how to modify the TiO_2 nanoparticles to lower the EA and IP* potentials in free charge carrier and S_1 exciton states, respectively, because, in practice, the thermodynamic driving force for the HER reaction will not be enough. Obvioulsy, it is very important to find a trend of the half-reaction potentials of TiO_2 nanoparticles studied here so that one would be able to predict the values of larger nanoparticles. However, unfortunately, we could not find any significant and consistent trend in those potentials as a function of size and/or shape. This is because the structural effect of small clusters studied here may be significant. However, we found weak size dependencies of IP_v and EA_v potentials.

To conclude this section we note that structural relaxation in the excited state is

responsible for significant change in the standard reduction potentials. It was found that stabilization energy values through structural relaxation in the S_1 exciton, free electron (anionic), and free hole (cationic) states in water are 0.3 – 1.0, 0.2 – 1.2, and 0.5 – 1.9 eV, respectively, at CAM-B3LYP/6-31G(d) level, indicating that the relaxation in the free hole state is the most significant. On the other hand, the shape dependence of the TiO_2 particles on the structural relaxation was also found to be significant. Upon structural relaxation in the excited states this leads to changes in the IP, EA, IP*, and EA* up to 1.9, 1.4, 1.5, and 0.7 eV, respectively, with concomitant changes in $IP_v^{(*)}/EA_v^{(*)}$ and $IP_{ad}^{(*)}/EA_{ad}^{(*)}$. The significant change in the standard reduction potentials induced by structural relaxation in the excited states highlights the importance of tracking adiabatic potential energy surface in the excited states.

5. Conclusions

We have studied the influence of the shape and size on the electronic structure of TiO_2 nanoparticles in a realistic 0.5-3.2 nm range using DFT and TD-DFT calculations using two types of hybrid functional and including solvent effects. The present results show that electronic structure is significantly more dependent on a nanoparticle's structure than its size. Hence, especially for the smaller nanoclusters, several different isomeric structures should be considered in order to evaluate the electronic structure and subsequently derived properties.

The calculation of relevant properties of TiO_2 nanoparticles indicates that, in the 0.5 - 3.2 nm range, the exciton binding energy is significant. This implies that the exciton state is thermodynamically significantly energetically favored over free charged species both in vacuum and in water for this size range. Tentative extrapolation of our results indicate that this is likely also to be the case for relatively large nanoparticles and that bulk like electronic behavior may be expected to emerge for ~6.5 nm diameter TiO_2

nanoparticles. The analysis of ionization potentials and electron affinities relative to the standard reduction potential for the HER and OER shows that the free charge carrier state of the TiO_2 nanoparticles studied here are able to drive photocatalytic water splitting, at least from a thermodynamic point of view. However, for the more stable exciton state, water splitting is only favored when the presence of water is taken into account although the approximate solvation model used implies that this conclusion needs to be taken with caution. Finally, we note that the present analysis provides necessary but not sufficient conditions for water splitting by photo-excited TiO_2 nanoparticles.

Acknowledgements

The authors are indebted to Prof. Peter Zapol for having made available the TB-DFT optimized structures reported in ref. 34 and to Prof. Martijn Zwinenburg for many valuable comments. This research was supported by the Spanish MINECO/FEDER CTQ2015-64618-R grant and, in part, by *Generalitat de Catalunya* (grants 2014SGR97 and XRQTC) and by the NOMAD Center of Excellence project, which received funding from the European Union's Horizon 2020 research and innovation programme under grant agreement No 676580. J.Y.L. acknowledges the financial support by Ministry of Science, ICT and Future Planning, subjected project to the project EDISON (Education-research Integration through Simulation On the Net, Grant No. 2012M3C1A6035359); K.C.K. acknowledges the financial support by Basic Science Research Program through the National Research Foundation of Korea (NRF) funded by the Ministry of Education (NRF-2014R1A6A3A03056449); O.L.G is grateful to the *Universitat de Barcelona* for a predoctoral grant; and, FI acknowledges additional support from the 2015 ICREA Academia Award for Excellence in University Research.Computational time at the Marenostrum supercomputer has been provided by the Barcelona Supercomputing Centre through grants from *Red Española de Supercomputación* and the COMPHOTOCAT project 2014112608 of the Partnership for Advanced Computing in Europe (PRACE).

Supporting Information.

The following information is available

1. Comparison between $(S_0 \rightarrow S_1)_v$ and $(S_0 \rightarrow T_1)$v excitations.
2. Energy per unit of the $(TiO_2)_n$ particles with n = 4,8,16, 35 and 84 as predicted from B3LYP/6-31G(d)/Water.
3. $\Delta E_{H\text{-}L}$(in eV) obtained at different level of theories.
4. Neutralization of Unique Charge Localization Patterns of Each Isomer upon Water Solvation.
5. Water splitting capabilities of TiO_2 NPs (IP/EA and IP*/EA* diagram) obtained at CAM-B3LYP/6-31G(d) level.
6. Excited state lifetime (τ) for vertical and relaxed S_1 excitons in vacuum and water.
7. Calculated electron and hole distributions in S_1 exciton and free charge carrier in vacuum and water obtained at the CAM-B3LYP/6-31G(d) level of theory.
8. Optimized geometries of neutral ground state and relaxed cationic, anionic, and adiabatic S_1 exciton states of $(TiO_2)_n$ with n = 4,8,16,35,84, in vacuum at CAM-B3LYP/6-31G(d) level.

This material is available free of charge via the Internet at http://pubs.acs.org.

Figure 1. Optimized structures of the four isomers of $(TiO_2)_4$, $(TiO_2)_8$ and $(TiO_2)_{16}$ studied (left) and the bulk cut structures for $(TiO_2)_{35}$ and $(TiO_2)_{84}$ (right). Relative total energies per TiO_2 unit are given with relative to that of the $(TiO_2)_{84}$ nanoparticle.

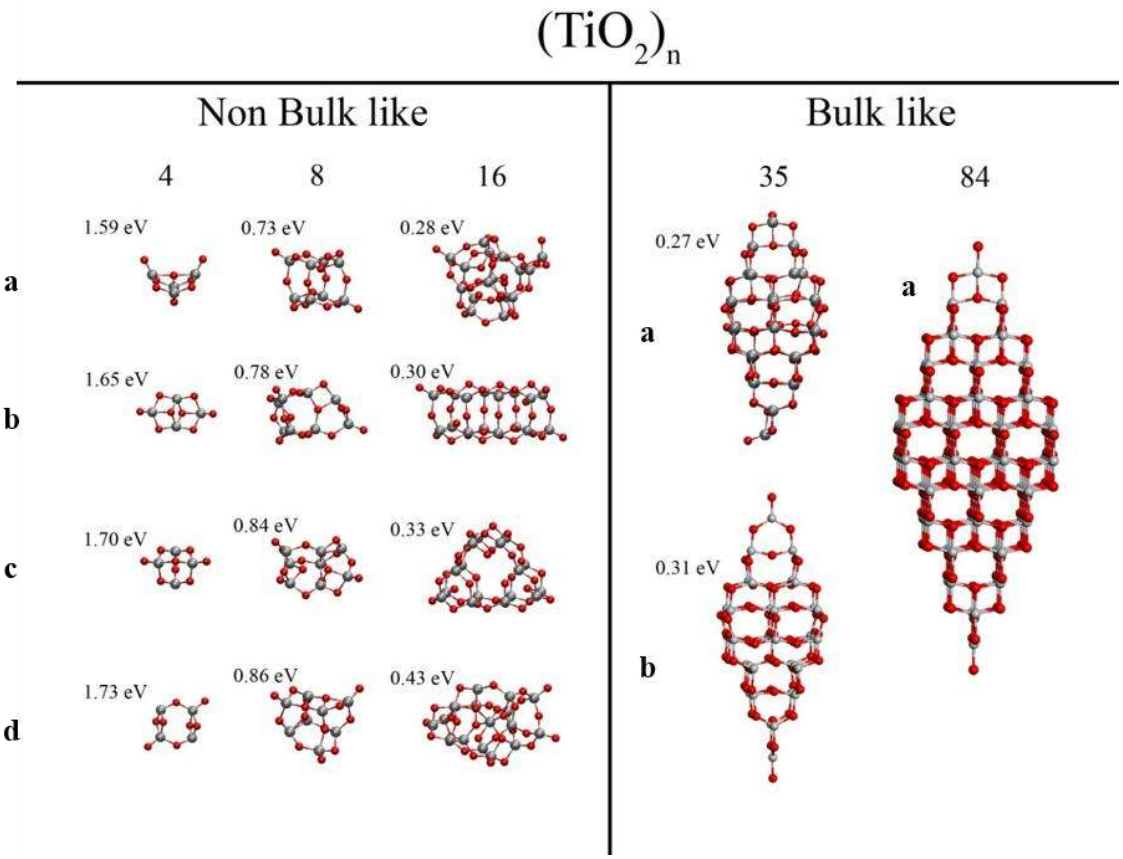

Figure 2. Energy per unit as a function of size for the lowest energy isomers of the $(TiO_2)_n$ particles with n = 4, 8, 16, 35 and 84 as predicted from B3LYP/6-31G(d) calculations. Structures are as in Figure 1 and the vertical shaded bars for particles with n = 4, 8 and 16 indicate the energy range spanned by the different isomers studied. The total energy per TiO_2 unit of the largest particle is taken to be zero.

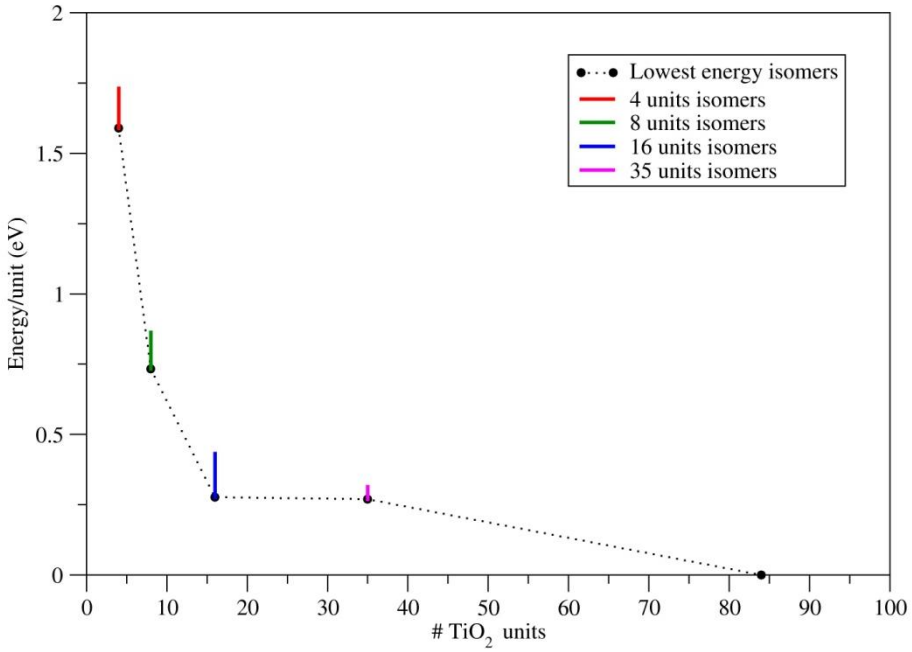

Figure 3. Optical (O_{gap}) energy gap (top panel) and electronic (E_{gap}) energy gap (bottom panel) of $(TiO_2)_4$, $(TiO_2)_8$, and $(TiO_2)_{16}$ cluster isomers (at a B3LYP/6-31G(d) level) and $(TiO_2)_{35}$, $(TiO_2)_{84}$ (at a B3LYP/6-31G(d)//PBE/tier-1 level) bulk cut nanoparticles in vacuum. Horizontal black and dashes lines indicates the experimental and B3LYP calculated[27] band gaps of bulk anatase. For the $(TiO_2)_4$, $(TiO_2)_8$, and $(TiO_2)_{16}$ particles, black, red, green, and blue colors correspond to results for isomers a, b, c, d, respectively. For $(TiO_2)_{35}$ black and red correspond to a and b isomers, respectively.

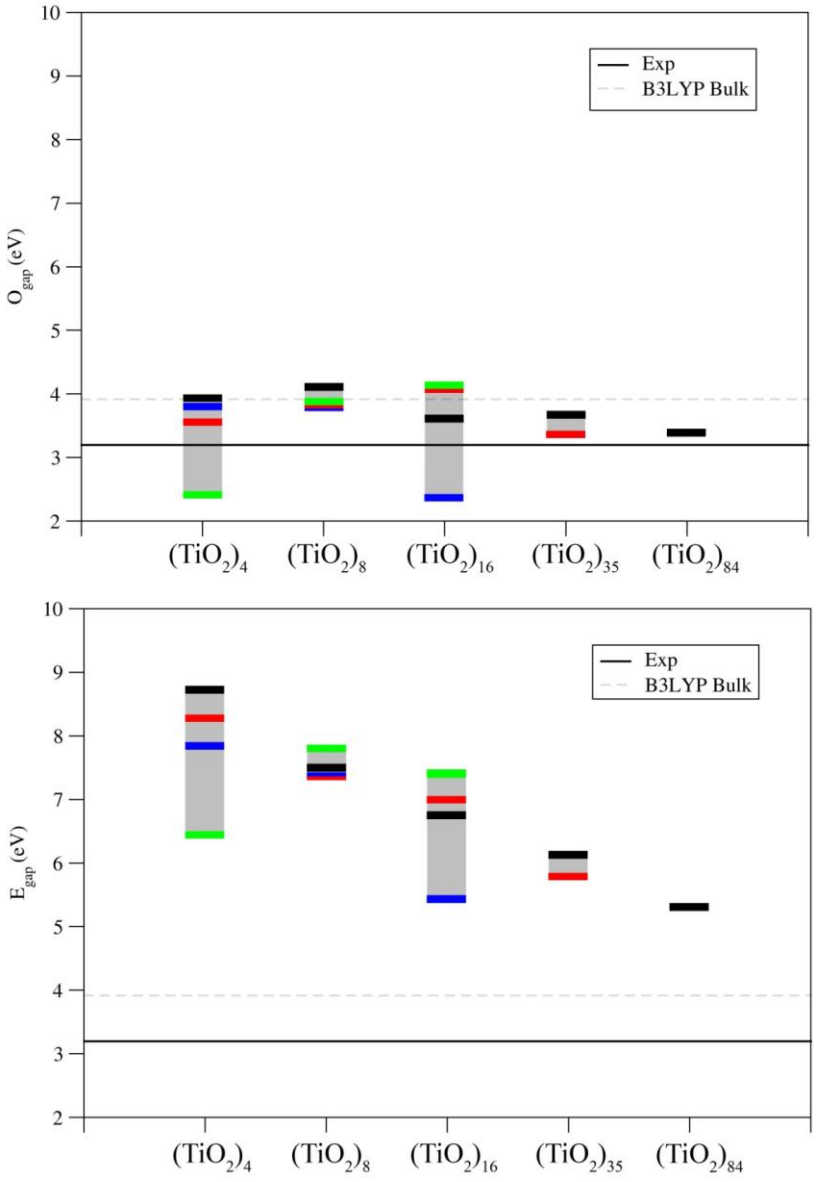

Figure 4. Optical (O_{gap}) energy gap (top panel) and electronic (E_{gap}) energy gap (bottom panel) of $(TiO_2)_4$, $(TiO_2)_8$, and $(TiO_2)_{16}$ cluster isomers (at a B3LYP/6-31G(d) level) and $(TiO_2)_{35}$, $(TiO_2)_{84}$ (at a B3LYP/6-31G(d)//PBE/tier-1 level) bulk cut nanoparticles in water. Horizontal black and dashes lines indicates the experimental and B3LYP calculated[27] band gaps of bulk anatase. For the $(TiO_2)_4$, $(TiO_2)_8$, and $(TiO_2)_{16}$ particles, black, red, green, and blue colors correspond to results for isomers a, b, c, d, respectively. For $(TiO_2)_{35}$ black and red correspond to a and b isomers, respectively.

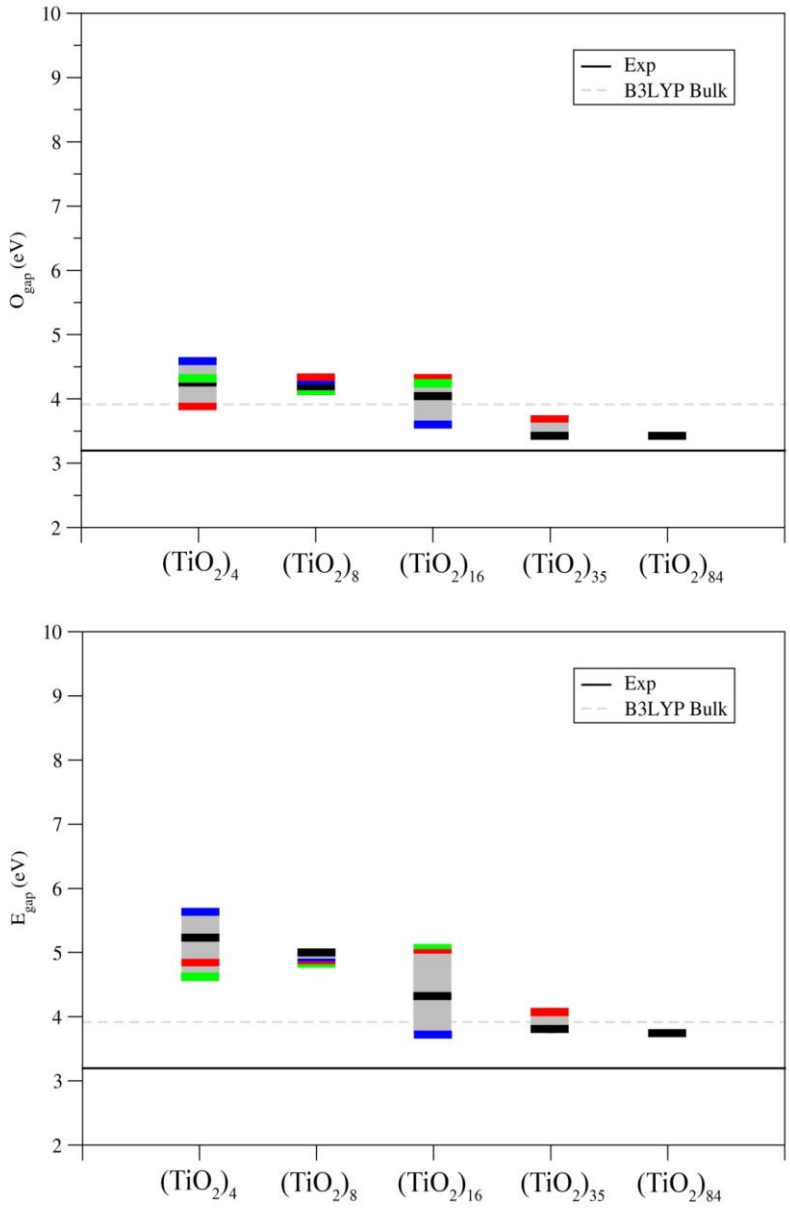

Figure 5a. Vertical (ΔE_{ex}) exciton binding energies with respect to the number of TiO_2 units in vacuum and water calculated at the B3LYP/6-31G(d) (top panels) and CAM-B3LYP/6-31G(d) (bottom panels) levels of theory. For the $(TiO_2)_{35}$ and the $(TiO_2)_{84}$ particles calculation correspond to the B3LYP/6-31G(d)//PBE/tier-1 level of theory. For the $(TiO_2)_4$, $(TiO_2)_8$, and $(TiO_2)_{16}$ particles, black, red, green, and blue colors correspond to results for isomers a, b, c, d, respectively. For $(TiO_2)_{35}$ black and red correspond to a and b isomers, respectively.

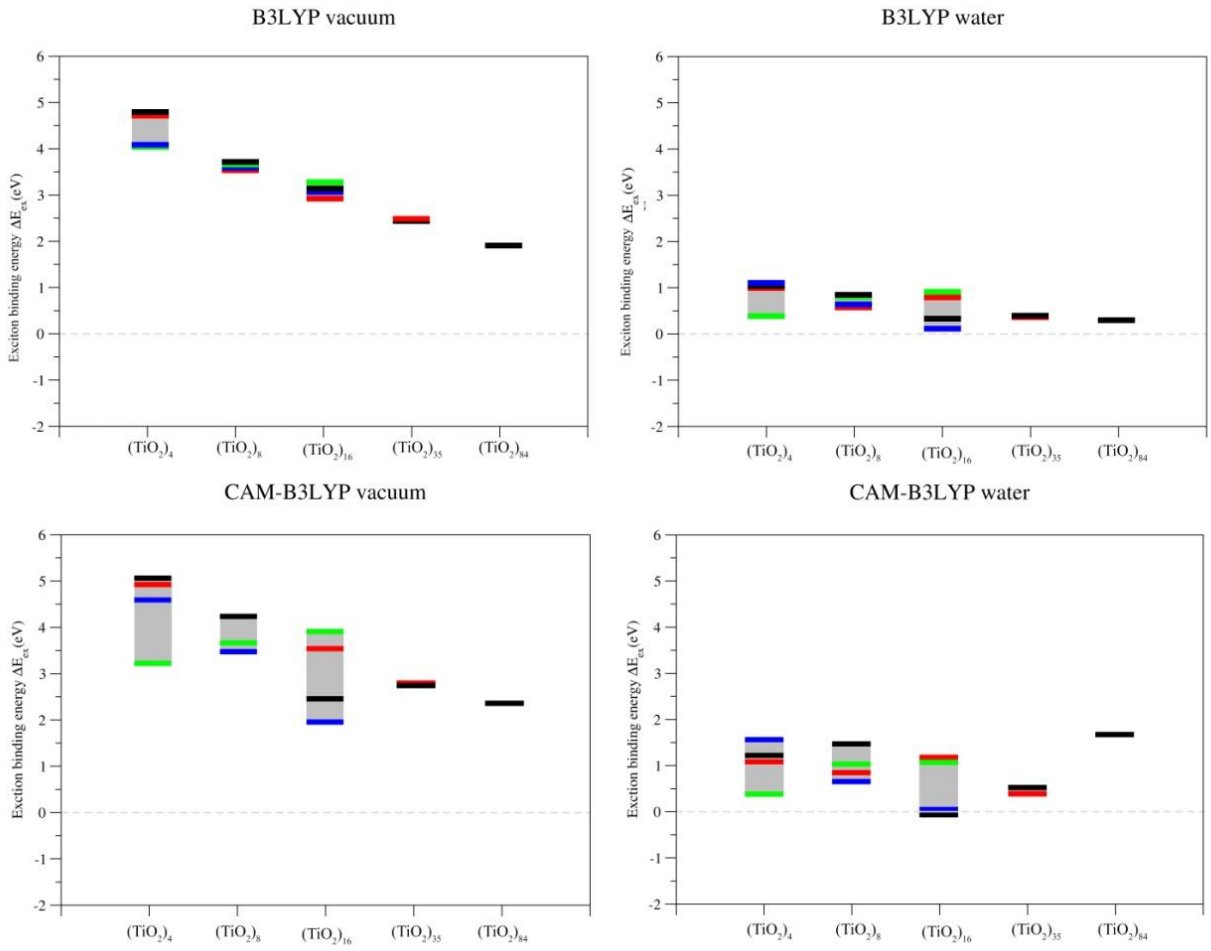

Figure 5b. Adiabatic (ΔE_{ex}) exciton binding energies with respect to the number of TiO_2 units in vacuum and water calculated at the CAM-B3LYP/6-31G(d) level. For the $(TiO_2)_4$, $(TiO_2)_8$, and $(TiO_2)_{16}$ particles, black, red, green, and blue colors correspond to results for isomers a, b, c, d, respectively.

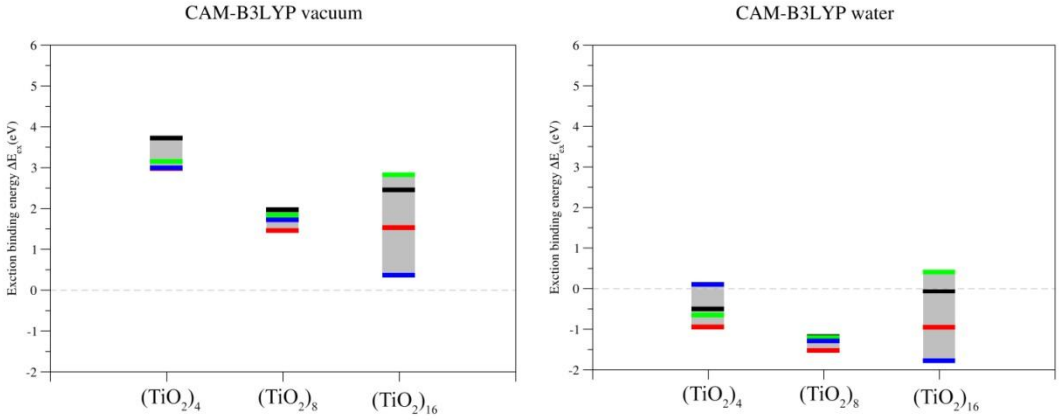

Figure 6. Variation of the vertical exciton binding energy $\Delta E_{ex,v}$ (in vacuum) with particle size from calculations at the B3LYP/6-31G(d) level. Top panel: $\Delta E_{ex,v}$ against size in number of TiO_2 units (n) with fit to the five data points, bottom panel: $\Delta E_{ex,v}$ against $n^{-0.3}$ with extrapolation to size for which $\Delta E_{ex,v}$(vacuum) = 0.2 eV. The blue dashed line in the bottom panel correspond to B3LYP values scaled down by 20% to correct for the known overestimate of the optical gap (see text).

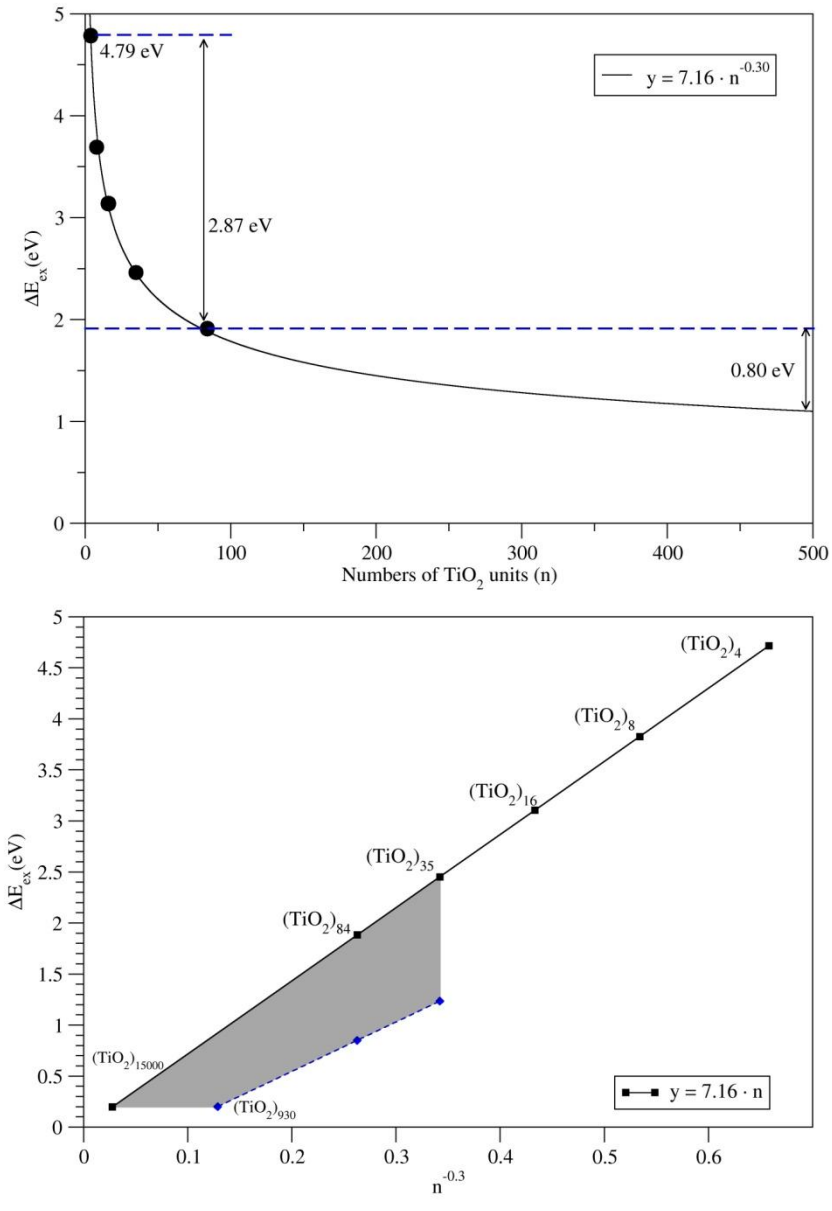

Figure 7. Schematic representation of standard reduction potentials in free charge carrier and S_1 exciton states for photocatalytic water splitting by TiO_2.

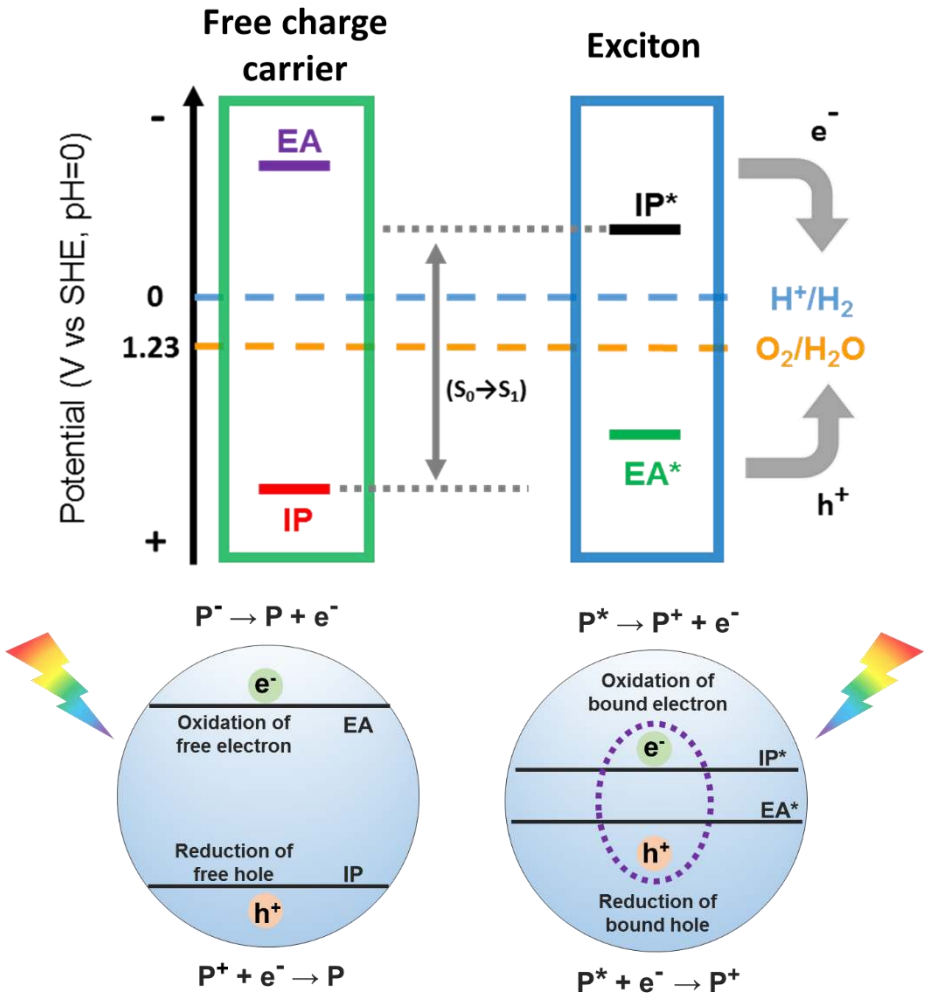

Figure 8. Calculated CAM-B3LYP/6-31G(d) vertical (top panel) and adiabatic (bottom panel) IP (triangles), EA (circles) of the TiO_2 nanoparticle free charge carrier (left) and S_1 exciton states (right) in water, relative to absolute value of the experimental SHE potential (4.44 eV). Potentials for HER (violet lines) and OER (orange lines) at pH = 0 (dashed lines) and pH = 7 (solid lines) are shown. Black, red, green, and blue colors correspond to results for isomers a, b, c, d, respectively.

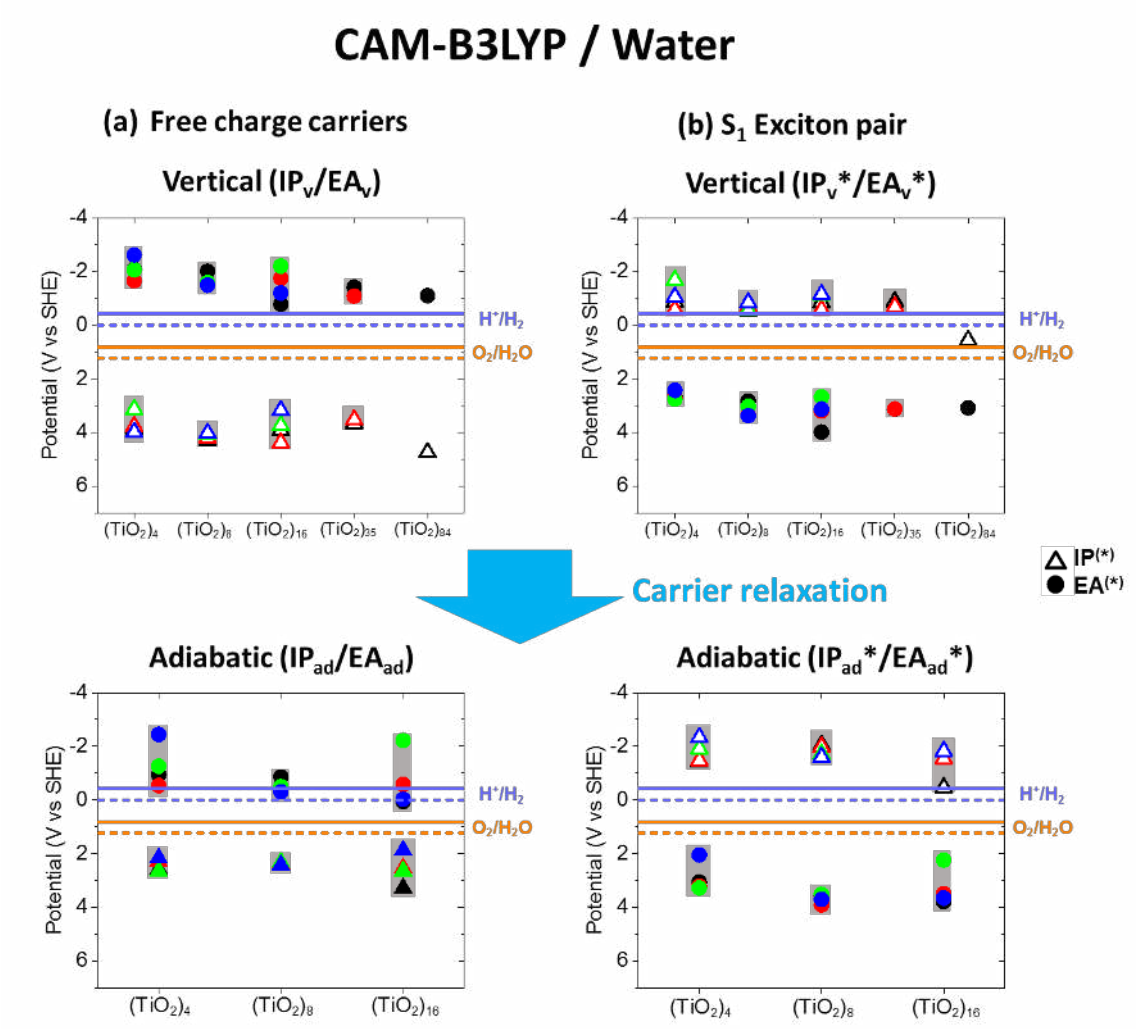

References

[1] Sousa, C.; Tosoni, S.; Illas, F. Theoretical Approaches to Excited-State-Related Phenomena in Oxide Surfaces. *Chem. Rev.* **2013**, *113*, 4456-4495.

[2] Henderson, M.A. A Surface Science Perspective on TiO_2 Photocatalysis. *Surf. Sci. Rep*. **2011**, *66*, 185-297.

[3] Diebold, U. The Surface Science of Titanium Dioxide. *Surf. Sci. Rep.* **2003**, *48*, 53-229

[4] Chen, X.; Mao, S. S. Titanium Dioxide Nanomaterials: Synthesis, Properties Modifications and Applications. *Chem. Rev.* **2007**, *107,* 2891–2959.

[5] Gratzel, M. Photoelectrochemical Cells. *Nature* **2001**, *414*, 338-344.

[6] Hagfeldt, A.; Boschloo, G.; Sun, L.; Kloo, L.; Pettersson, H. Dye-Sensitized Solar Cells. *Chem. Rev.* **2010**, *110*, 6595-6663.

[7] Hoffmann, M. R.; Martin, S. T.; Choi, W.; Bahnemann, D. W. Environmental Applications of Semiconductor Photocatalysis. *Chem. Rev*. **1995**, *95,* 69–96.

[8] Mill, A.; Davies, R. H.; Worsley, D. Water-Purification by Semiconductor Photocatalysis. *Chem. Soc. Rev.* **1993**, *22*, 417–425.

[9] Fox, M. A.; Dulay, M. T. Heterogeneous Photocatalysis. *Chem. Rev.* **1993**, *93*, 341–357.

[10] Xu, H.; Ouyang, S.; Liu, L.; Reunchan, P.; Umezawa, N.; Ye, J. Recent Advances in TiO_2-based Photocatalysis. *J. Mater. Chem. A* **2014**, *2*, 12642−12661.

[11] Hashimoto, K.; Irie, H.; Fujishima, A. TiO_2 Photocatalysis: A Historical Overview and Future Prospects. *Jpn. J. Appl. Phys*. **2005**, *44*, 8269–8285.

[12] Fujishima, A.; Zhang, X.; Tryk, D. A. TiO_2 Photocatalysis and Related Surface Phenomena. *Surf. Sci. Rep*. **2008**, *63,* 515–582.

[13] Chen, X. B.; Shen, S. H.; Guo, L. J.; Mao,S. S. Semiconductor-Based Photocatalytic Hydrogen Generation. *Chem. Rev.* **2010***, 110*, 6503–6570.

[14] Kudo, A.; Miseki, Y. Heterogeneous Photocatalyst Materials for Water Splitting. *Chem. Soc. Rev.* **2009**, *38*, 253–278.

[15] Kavan, L.; Gratzel, M.; Gilbert, S. E.; Klemenz, C.; Scheel, H. J. Electrochemical and Photoelectrochemical Investigation of Single-Crystal Anatase. *J. Am. Chem. Soc.* **1996**, *118*, 6716-6723.

[16] Asahi, R.; Morikawa, T.; Ohwaki, T.; Aoki, K.; Taga, Y. Visible-light Photocatalysis in Nitrogen-doped Titanium Oxides. *Science* **2001**, *293*, 269-271.

[17] Asahi, R.; Morikawa, T.; Irie, H.; Ohwaki, T. Nitrogen-Doped Titanium Dioxide as Visible-Light-Sensitive Photocatalyst: Designs, Developments, and Prospects. *Chem. Rev.* **2014**, *114*, 9824-9852.

[18] Di Valentin, C.; Pacchioni, G. Spectroscopic Properties of Doped and Defective Semiconducting Oxides from Hybrid Density Functional Calculations. *Acc. Chem. Res.* **2014**, *47*, 3233-3241.

[19] Calatayud, D.; Jardiel, T.; Peiteado, M.; Illas, F.; Giamello, E.; Palomares, F.; Fernández Hevia, D.; Caballero, A. Synthesis and characterization of blue faceted anatase nanoparticles through extensive fluorine lattice doping. *J. Phys. Chem. C* **2015**, *119*, 21243-21250

[20] Liu, G.; Yang, H. G.; Pan, J.; Yang, Y. Q.; Lu, G. Q. (Max); Cheng, H. M. Titanium Dioxide Crystals with Tailored Facets. *Chem. Rev.* **2014**, *114*, 9559-9612.

[21] Yang, H. G.; Sun, C. H.; Qiao, S. Z.; Zou, J.; Liu, G.; Smith, S. C.; Cheng, H. M.; Lu, G. Q. Anatase TiO_2 single crystals with a large percentage of reactive facets. *Nature* **2008**, *453*, 638-641

[22] Lamiel-Garcia, O.; Tosoni, S.; Illas, F. Relative stability of F covered TiO_2 anatase (101) and (001) surfaces from periodic DFT calculations and ab initio

atomistic thermodynamics. *J. Phys. Chem. C* **2014**, 118, 13667-13673.

[23] Mattioli, G.; Filippone, F.; Alippi, P.; Amore Bonapasta, A. Ab Initio Study of the Electronic States Induced by Oxygen Vacancies in Rutile and Anatase TiO_2. *Phys. Rev. B* **2008**, *78*, 241201.

[24] Morgan, B. J.; Watson, G. W. Intrinsic n-type Defect Formation in TiO_2: A Comparison of Rutile and Anatase from GGA+U Calculations. *J. Phys. Chem. C* **2010**, *114*, 2321-2328.

[25] Stausholm-Møller, J.; Kristoffersen, H. H.; Hinnemann, B.; Madsen, G. K. H.; Hammer, B. DFT+U Study of Defects in Bulk Rutile TiO_2. *J. Chem. Phys.* **2010**, *133*, 144708.

[26] Mattioli, G.; Alippi, P.; Filippone, F.; Caminiti, R.; Amore Bonapasta, A. Deep versus Shallow Behavior of Intrinsic Defects in Rutile and Anatase TiO_2 Polymorphs. *J. Phys. Chem. C* **2010**, *114*, 21694-21704.

[27] Finazzi, E.; Di Valentin, C.; Pacchioni, G.; Selloni, A. Excess electron states in reduced bulk anatase TiO_2: Comparison of standard GGA, GGA+U, and hybrid DFT calculations. *J. Chem. Phys.* **2008**, *129*, 154113.

[28] Islam, M. M.; Bredow, T.; Gerson, A. Electronic properties of oxygen-deficient and aluminum-doped rutile TiO_2 from first principles. *Phys. Rev. B* **2007**, *76*, 045217.

[29] Janotti, A.; Varley, J. B.; Rinke, P.; Umezawa, N.; Kresse, G.; Van de Walle, C. G. Hybrid Functional Studies of the Oxygen vacancy in TiO_2. *Phys. Rev. B* **2010**, *81*, 085212.

[30] Deák, P.; Aradi, B.; Frauenheim, T. Quantitative Theory of the Oxygen Vacancy and Carrier Self-Trapping in Bulk TiO_2. *Phys. Rev. B* **2012**, *86*, 195206.

[31] Lazzeri, M.; Vittadini, A.; Selloni, A. Structure and energetics of stoichiometric

TiO_2 anatase surfaces. *Phys. Rev. B* **2001**, *63*, 155409.

[32] Gong, X. Q.; Selloni, A. Reactivity of anatase TiO_2 nanoparticles: The role of the minority (001) surface. *J. Phys. Chem. B* **2005**, *109*, 19560-19562.

[33] Morgan, B. J.; Watson, G. W. A DFT+U description of oxygen vacancies at the TiO_2 rutile (110) surface. *Surf. Sci.* **2007**, *601*, 5034-5041.

[34] Barnard, A. S.; Erdin, S.; Lin, Y.; Zapol, P.; Halley, J. W. Modeling the Structure and Electronic Properties of TiO_2 Nanoparticles. *Phys. Rev. B* **2006**, *73*, 205405.

[35] Auvinen, S.; Alatalo, M.; Haario, H.; Jalava, J. P.; Lamminmäki, R. J. Size and Shape Dependence of the Electronic and Spectral Properties in TiO_2 Nanoparticles. *J. Phys. Chem. C* **2011**, *115*, 8484-8493.

[36] Hamad, S.; Catlow, C. R.A; Woodley, S. M.; Lago, S.; Mejias, J. A. Structure and stability of small TiO_2 nanoparticles. *J. Phys. Chem. B* **2005**, 109, 15741-15748.

[37] Syzgantseva, O. A.; Gonzalez-Navarrete, P.; Calatayud, M.; Bromley, S.; Minot, C. Theoretical Investigation of the Hydrogenation of $(TiO_2)_n$ Clusters (n= 1–10). *J. Phys. Chem. C* **2011**, 115, 15890-15899.

[38] Marom, N.; Kim, M.; Chelikowsky, J. R. Structure Selection Based on High Vertical Electron Affinity for TiO_2 Clusters. *Phys. Rev. Lett.* **2012**, 108, 106801.

[39] Chen, M. Y.; Dixon, D. A. Tree Growth-Hybrid Genetic Algorithm for Predicting the Structure of Small $(TiO_2)_n$, n=2-13, Nanoclusters. *J. Chem. Theory Comput.* **2013**, *9*, 3189-3200.

[40] Buckeridge, J.; Butler, K. T.; Catlow, C. R. A.; Logsdail, A. J.; Scanlon, D. O.; Shevlin, S. A.; Woodley, S. M.; Sokol, A. A.; Walsh, A. Polymorph Engineering of TiO_2: Demonstrating How Absolute Reference Potentials Are Determined by Local Coordination. *Chem. Mater.* **2015**, *27*, 3844–3851.

[41] Shevlin, S. A.; Woodley, S. M. Electronic and Optical Properties of Doped and

Undoped $(TiO_2)_n$ Nanoparticles. *J. Phys. Chem. C* **2010**, *114*, 17333-17343

[42] Berardo, E.; Hu, H. S.; Shevlin, S. A.; Woodley, S. M.; Kowalski, K.; Zwijnenburg, M. A. Modeling Excited States in TiO_2 Nanoparticles: On the Accuracy of a TD-DFT Based Description. *J. Chem. Theory Comput.* **2014**, *10*, 1189-1199.

[43] Bredas, J. L. Mind the gap! *Mater. Horiz.* **2014**, *1*, 17-19.

[44] Pascual, J.; Camassel, J.; Mathieu, H. Fine Structure in the Intrinsic Absorption Edge of TiO_2. *Phys. Rev. B* **1978**, *18*, 5606–5614.

[45] Tang, H.; Levy, F.; Berger, H.; Schmid, P. E. Urbach tail of anatase TiO_2, *Phys. Rev. B* **1995**, *52*, 7771-7774.

[46] Kang, W. ; Hybertsen, M. S. Quasiparticle and Optical Properties of Rutile and Anatase TiO_2. *Phys. Rev. B* **2010**, *82*, 085203.

[47] Guiglion, P.; Butchosa, C.; Zwijnenburg, M. Polymeric watersplitting photocatalysts; a computational perspective on the water oxidation conundrum. *J. Mater. Chem. A* **2014**, 2, 11996-12004.

[48] Berardo, E.; Hu, H. S.; van Dam, H. J. J.; Shevlin, S. A.; Woodley, S. M.; Kowalski, K.; Zwijnenburg, M. A. Describing excited state relaxation and localization in TiO_2 nanoparticles using TD-DFT. *J. Chem. Theory Comput.* **2014**, *10*, 5538-5548.

[49] Guiglion, P.; Berardo, E.; Butchosa, C.; Wobbe, M. C. C.; Zwijnenburg, M. A. Modelling materials for solar fuel synthesis by artificial photosynthesis; predicting the optical, electronic and redox properties of photocatalysts. *J. Phys.: Condens. Matter* **2016**, *28*, 074001.

[50] Becke, A. D. Density-Functional Thermochemistry. III. The Role of Exact Exchange. *J. Chem. Phys.***1993**, *98*, 5648.

[51] Yanai, T.; Tew, D. P.; Handy, N. C. A New Hybrid Exchange–correlation Functional Using the Coulomb-Attenuating Method (CAM-B3LYP). *Chem. Phys. Lett.* **2004**, *393*, 51–57.

[52] Frisch, M. J.; Trucks, G. W.; Schlegel, H. B.; Scuseria, G. E.; Robb, M. A.; Cheeseman, J. R.; Scalmani, G.; Barone, V.; Mennucci, B.; Petersson, G. A.; Nakatsuji, H.; Caricato, M.; Li, X.; Hratchian, H. P.; Izmaylov, A. F.; Bloino, J.; Zheng, G.; Sonnenberg, J. L.; Hada, M.; Ehara, M.; Toyota, K.; Fukuda, R.; Hasegawa, J.; Ishida, M.; Nakajima, T.; Honda, Y.; Kitao, O.; Nakai, H.; Vreven, T.; Montgomery, J. A., Jr.; Peralta, J. E.; Ogliaro, F.; Bearpark, M.; Heyd, J. J.; Brothers, E.; Kudin, K. N.; Staroverov, V. N.; Kobayashi, R.; Normand, J.; Raghavachari, K.; Rendell, A.; Burant, J. C.; Iyengar, S. S.; Tomasi, J.; Cossi, M.; Rega, N.; Millam, J. M.; Klene, M.; Knox, J. E.; Cross, J. B.; Bakken, V.; Adamo, C.; Jaramillo, J.; Gomperts, R.; Stratmann, R. E.; Yazyev, O.; Austin, A. J.; Cammi, R.; Pomelli, C.; Ochterski, J. W.; Martin, R. L.; Morokuma, K.; Zakrzewski, V. G.; Voth, G. A.; Salvador, P.; Dannenberg, J. J.; Dapprich, S.; Daniels, A. D.; Farkas, Ö.; Foresman, J. B.; Ortiz, J. V.; Cioslowski, J.; Fox, D. J. *Gaussian 09*, Revision D.01; Gaussian, Inc.: Wallingford, CT, 2013.

[53] Wales, D. J.; Doye, J. P. K. Global Optimization by Basin-Hopping and the Lowest Energy Structures of Lennard-Jones Clusters Containing up to 110 Atoms. *J. Phys. Chem. A* **1997**, *101*, 5111-5116.

[54] Wulff, G. On the question of speed of growth and dissolution of crystal surfaces. *Z. Krist.* **1901**, *34*, 449-530.

[55] Blum, V.; Gehrke, R.; Hanke, F.; Havu, P.; Havu, V.; Ren, X.; Reuter, K.; Scheffler, M. Ab Initio Molecular Simulations with Numeric Atom-Centered Orbitals. *Comput. Phys. Commun.* **2009**, *180*, 2175–2196.

[56] Hirata, S.; Head-Gordon, M. Time-Dependent Density Functional Theory within the Tamm–Dancoff Approximation. *Chem. Phys. Lett.* **1999**, *314*, 291–299.

[57] Tomasi, J.; Persico, M. Molecular Interactions in Solution: An Overview of Methods Based on Continuous Distributions of the Solvent. *Chem. Rev.* **1994**, *94*, 2027–2094.

[58] Pandey, L. B.; Aikens, C. M. Theoretical Investigation of the Electrochemical Mechanism of Water Splitting on a Titanium Oxide Cluster Model. *J. Phys. Chem. A* **2012**, *116*, 526–535.

[59] De Angelis, F.; Fantacci, S.; Gebauer, R. Simulating Dye-Sensitized TiO_2 Heterointerfaces in Explicit Solvent: Absorption Spectra, Energy Levels, and Dye Desorption. *J. Phys. Chem. Lett.* **2011**, *2*, 813–817.

[60] Di Valentin, C.; Pacchioni, G.; Selloni, A. Electronic Structure of Defect States in Hydroxylated and Reduced Rutile TiO_2 (110) Surfaces. *Phys. Rev. Lett.* **2006**, *97*, 166803.

[61] Bromley, S. T.; Moreira, I. De P.R.; Neyman, K-M.; Illas, F. Approaching nanoscale oxides: models and theoretical methods. *Chem. Soc. Rev.* **2009**, *38*, 2657-2670.

[62] Persson, P; Gebhardt, J. C. M.; Lunell, S. The Smallest Possible Nanocrystals of Semiionic Oxides. *J. Phys. Chem. B* **2003**, *107*, 3336-3339.

[63] Manzhos, S.; Segawa, H.; Yamashita, K. Computational Dye Design by Changing the Conjugation Order: Failure of LR-TDDFT to Predict Relative Excitation Energies in Organic Dyes Differing by the Position of the Methine Unit. *Chem. Phys. Lett.* **2012**, *527*, 51–56.

[64] Berardo, E.; Zwijnenburg, M. A. Modeling the Water Splitting Activity of a TiO_2 Rutile Nanoparticle. *J. Phys. Chem. C* **2015**, *119*, 13384–13393.

[65] Xu, M.; Gao, Y.; Moreno, E. M.; Kunst, M.; Muhler, M.; Wang, Y.; Idriss, H.; Wöll, C. Photocatalytic Activity of Bulk TiO_2 Anatase and Rutile Single Crystals Using Infrared Absorption Spectroscopy. *Phys. Rev. Lett.* **2011**, *106*, 138302.

[66] Tamaki, Y.; Furube, A.; Murai, M.; Hara, K.; Katoh, R.; Tachiya, M. Dynamics of Efficient Electron-Hole Separation in TiO_2 Nanoparticles Revealed by Femtosecond Transient Absorption Spectroscopy under the Weak-Excitation Condition. *Phys. Chem. Chem. Phys.* **2007**, *9*, 1453–1460.

[67] Tamaki, Y.; Hara, K.; Katoh, R.; Tachiya, M.; Furube, A. Femtosecond Visible-to-IR Spectroscopy of TiO_2 Nanocrystalline Films: Elucidation of the Electron Mobility before Deep Trapping. *J. Phys. Chem. C* **2009**, *113*, 11741–11746.

[68] Barnard, A. S.; Zapol, P. Predicting the Energetics, Phase Stability, and Morphology Evolution of Facted and Spherical Anatase Nanocrystals, *J. Phys. Chem. B*, **2004**, 108, 18435-18440.

[69] Moreira, I. de P. R.; Illas, F.; Martin, R. L. Effect of Fock exchange on the electronic structure and magnetic coupling in NiO *Phys. Rev. B*, **2002**, *65*, 155102.

[70] Guiglion, P.; Berardo, E.; Butchosa, C.; Wobbe, M. C. C.; Zwijnenburg, M. A. Modelling Materials for Solar Fuel Synthesis by Artificial Photosynthesis; Predicting the Optical, Electronic and Redox Properties of Photocatalysts. *J. Phys. Condens. Matter* **2016**, *28*, 74001.

[71] Guiglion, P.; Butchosa, C.; Zwijnenburg, M. A. Polymer Photocatalysts for Water Splitting: Insights from Computational Modeling. *Macromol. Chem. Phys.* **2016**, *217*, 344–353.

[72] Nunzi, F.; Agrawal, S.; Selloni, A.; De Angelis, F. Structural and Electronic

Properties of Photoexcited TiO_2 Nanoparticles from First Principles. *J. Chem. Theory Comput.* **2015**, *11*, 635–645.

[73] Trasatti, S. The Absolute Electrode Potential: An Explanatory Note. *Pure Appl. Chem*. **1986**, *58*, 955–966.

[74] Trasatti, S. The Concept of Absolute Electrode Potential an Attempt at a Calculation. *J. Electroanal. Chem.* **1974**, *52*, 313–329.

[75] Scanlon, D. O.; Dunnill, C. W.; Buckeridge, J.; Shevlin, S. A.; Logsdail, A. J.; Woodley, S. M.; Catlow, C. R. A.; Powell, M. J.; Palgrave, R. G.; Parkin, I. P.; Watson, G. W.; Keal, T. W.; Sherwood, P.; Walsh, A.; Sokol, A. A. Band Alignment of Rutile and Anatase TiO_2. *Nat. Mater.* **2013**, *12*, 798–801.

[76] Stevanovic, V.; Lany, S.; Ginley, D. S.; Tumas, W.; Zunger, A. Assessing Capability of Semiconductors to Split Water Using Ionization Potentials and Electron Affinities Only. *Phys. Chem. Chem. Phys.* **2014**, *16*, 3706–3714.

Graphic for TOC